
Gradient-Direction-Aware Density Control for 3D Gaussian Splatting

Zheng Zhou

Shanghai University of Engineering Science
Shanghai 201620, China
m320123332@sues.edu.cn

Yu-Jie Xiong

Shanghai University of Engineering Science
Shanghai 201620, China
xiong@sues.edu.cn

Chun-Ming Xia

Shanghai University of Engineering Science
Shanghai 201620, China
cmxia@sues.edu.cn

Jia-Chen Zhang

Shanghai University of Engineering Science
Shanghai 201620, China
m325123603@sues.edu.cn

Hong-Jian Zhan

East China Normal University
Shanghai 200241, China
hjzhan@cee.ecnu.edu.cn

Abstract

The emergence of 3D Gaussian Splatting (3DGS) has significantly advanced novel view synthesis through explicit scene representation, enabling real-time photorealistic rendering. However, existing approaches manifest two critical limitations in complex scenarios: (1) Over-reconstruction occurs when persistent large Gaussians cannot meet adaptive splitting thresholds during density control. This is exacerbated by conflicting gradient directions that prevent effective splitting of these Gaussians; (2) Over-densification of Gaussians occurs in regions with aligned gradient aggregation, leading to redundant component proliferation. This redundancy significantly increases memory overhead due to unnecessary data retention. We present Gradient-Direction-Aware Gaussian Splatting (GDAGS), a gradient-direction-aware adaptive density control framework to address these challenges. Our key innovations: the gradient coherence ratio (GCR), computed through normalized gradient vector norms, which explicitly discriminates Gaussians with concordant versus conflicting gradient directions; and a nonlinear dynamic weighting mechanism leverages the GCR to enable gradient-direction-aware density control. Specifically, GDAGS prioritizes conflicting-gradient Gaussians during splitting operations to enhance geometric details while suppressing redundant concordant-direction Gaussians. Conversely, in cloning processes, GDAGS promotes concordant-direction Gaussian densification for structural completion while preventing conflicting-direction Gaussian overpopulation. Comprehensive evaluations across diverse real-world benchmarks demonstrate that GDAGS achieves superior rendering quality while effectively mitigating over-reconstruction, suppressing over-densification, and constructing compact scene representations with 50% reduced memory consumption through optimized Gaussians utilization. Our code can be accessed in the code repository <https://github.com/zzcqz/GDAGS>.

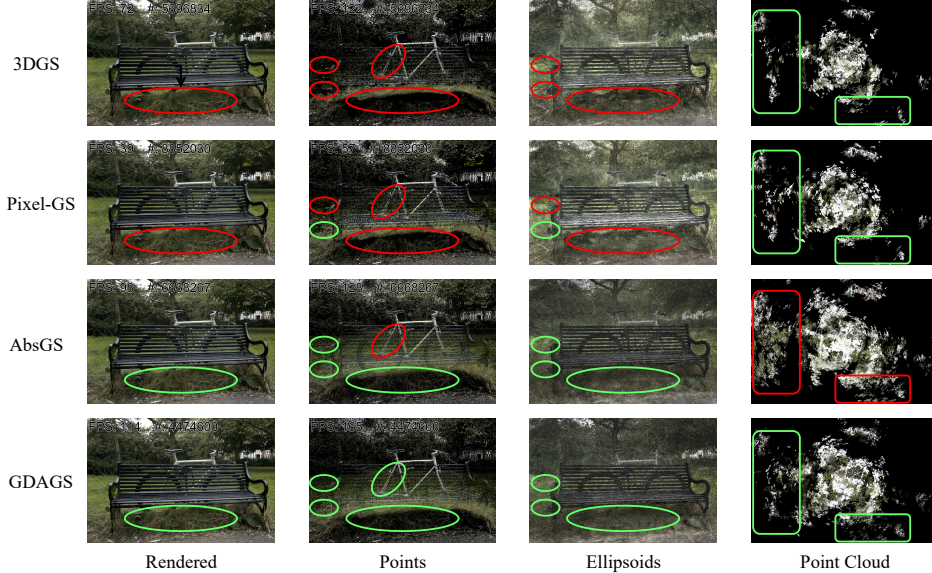


Figure 1: Visualization of rendering performance and efficiency, with rendering frame rate and scene Gaussian count displayed in the upper left corner. The green box represents the optimized area, and the red box represents the poorly optimized area. Both GDAGS and AbsGS effectively densify and eliminate large Gaussians in over-reconstructed areas to restore fine details. However, AbsGS has too many over-densification Gaussians, which only contribute slightly to rendering quality. In contrast, GDAGS has a more compact and reasonable spatial distribution and only requires half of the Gaussians in Pixel-GS.

1 Introduction

Novel View Synthesis (NVS) constitutes a foundational challenge in computer graphics and vision, aiming to reconstruct 3D scenes from monocular images to generate photorealistic novel perspectives. While neural implicit representations, such as Neural Radiance Fields (NeRF) [1], have significantly advanced NVS by modeling radiation fields through multilayer perceptrons (MLPs) and volumetric rendering, these methods struggle to reconcile rendering quality [2] with computational efficiency [3]. Emerging as a novel paradigm, 3D Gaussian Splatting [4] explicitly parameterizes scenes using adaptive Gaussian primitives. By integrating splat-based rasterization with adaptive density control strategies, 3DGS achieves real-time rendering of unprecedented fidelity while maintaining compact spatial representation.

However, the adaptive density control mechanism in 3DGS exhibits inherent limitations. Specifically, 3DGS’s densification criterion solely relies on the norm of view-space positional gradients, thereby overlooking the directional influence of gradients on the norm computation. During view-space positional gradient calculation for each Gaussian, the superposition of sub-gradient components with consistent directions amplifies the gradient norm. Conversely, counter-directional sub-gradient components mutually attenuate, resulting in reduced gradient norms. These directional conflicts prevent some Gaussians from effective densification, causing over-reconstruction phenomenon and perceptible local blurring. Meanwhile, Gaussians maintaining consistent gradient directions exhibit persistent densification tendencies, causing over-densification phenomena that generate redundant Gaussian primitives and significantly increase memory consumption. Recent work like AbsGS [5] has proposed using absolute subgradient values to enforce positive gradients for all Gaussians, thereby avoiding subgradient directional conflicts and partially mitigating the over-reconstruction issue. This approach further exacerbates the over-densification phenomenon, as shown in Figure 1.

To address the aforementioned dual challenges, we propose a gradient-direction-aware adaptive density control framework (GDAGS). This approach combines directional subgradient information and gradient magnitude data to establish a novel decision metric. The metric enables controlled densification of Gaussians with conflicting directional gradients while preventing redundant densification in directionally aligned cases. First, GDAGS calculates a normalized GCR to measure the directional consistency of subgradients for each Gaussian. The GCR value approaching 1 indicates highly

consistent subgradient directions, whereas a value approaching 0 signifies substantial directional conflict. Subsequently, GDAGS employs GCR to parameterize a nonlinear dynamic weight w_i , which independently weights the view-space positional gradients of each Gaussian to form a new decision metric controlling densification behavior. During splitting operations, Gaussians exhibiting directional conflicts receive higher weights and are prioritized for splitting, while directionally consistent Gaussians obtain lower weights and are suppressed. Finally, GDAGS introduces a hyperparameter p to explicitly control the number of Gaussians participating in densification, thereby achieving an indirect balance between performance and efficiency. We summarize our contributions as follows:

- We utilize GCR as a gradient direction consistency measure for adaptive density control to identify Gaussians with consistent and divergent directions.
- We propose a nonlinear dynamic weighting mechanism to independently weight the Gaussians in the scene, promoting correct densification and suppressing abnormal densification of the Gaussians.
- Evaluated on three real-world datasets spanning 13 scenes, our method demonstrated superior visual quality while having a compact spatial representation that requires only 50% Gaussians and memory consumption.

2 Related work

2.1 Novel view synthesis

Novel View Synthesis has evolved through two interconnected trajectories: advancements in scene representation paradigms and optimizations of rendering efficiency. The field was revolutionized by NeRF [1], which introduced MLP-based implicit neural representations to map spatial coordinates to radiance and density values, achieving photorealistic results through volumetric rendering. However, NeRF’s computational demands spurred research bifurcating into quality refinement and efficiency optimization. Approaches like Mip-NeRF [6] enhanced geometric stability using conical ray encoding and distortion regularization, while DVGO [7] and Instant-NGP [8] leveraged explicit 3D grids and hash encoding to achieve near-real-time rendering. This progression culminated in 3D Gaussian Splatting [4], which redefined the paradigm by combining explicit Gaussian primitives with differentiable rasterization. By parameterizing scenes as adaptive 3D Gaussians, 3DGS bridged the gap between implicit continuity and explicit computational efficiency, achieving rendering speeds two orders of magnitude faster than NeRF while maintaining visual parity with state-of-the-art methods like Mip-NeRF360 [9].

2.2 3D gaussian splatting

The rapid adoption of 3DGS has driven innovations addressing its inherent limitations. Early improvements focused on geometric fidelity: Mip-Splatting [10] integrated multi-scale primitives and low-pass filtering to mitigate aliasing, while GOF [11] introduced composite gradient metrics to optimize Gaussian distributions. Subsequent methods explored structural constraints, such as 2DGSs [12] planar surface projections and RadeGSs [13] normal map-guided refinement. Frequency-aware approaches like FreGS [14] employed spectral regularization to enhance high-frequency detail recovery, whereas HoGS [15] utilized homogeneous coordinate reparameterization to improve distant object reconstruction. Despite these advances, critical challenges persist in adaptive density control. ABSGS [5] enforced gradient direction uniformity to resolve over-reconstruction but indiscriminately amplified outliers, while PixelGS [16] traded memory efficiency for geometric precision by weighting gradients via pixel coverage—a strategy incurring prohibitive storage costs and frame rate penalties. Our work addresses these unresolved trade-offs through directional gradient awareness, systematically balancing precision, efficiency, and memory constraints.

3 Method

Section 3.1 establishes the methodological motivation for GDAGS, and Section 3.2 outlines 3DGS fundamentals. Sections 3.3.1 and 3.3.2 detail GDAGS’ core components, with full algorithmic implementation provided in Appendix A. The complete pipeline is shown in Figure 2.

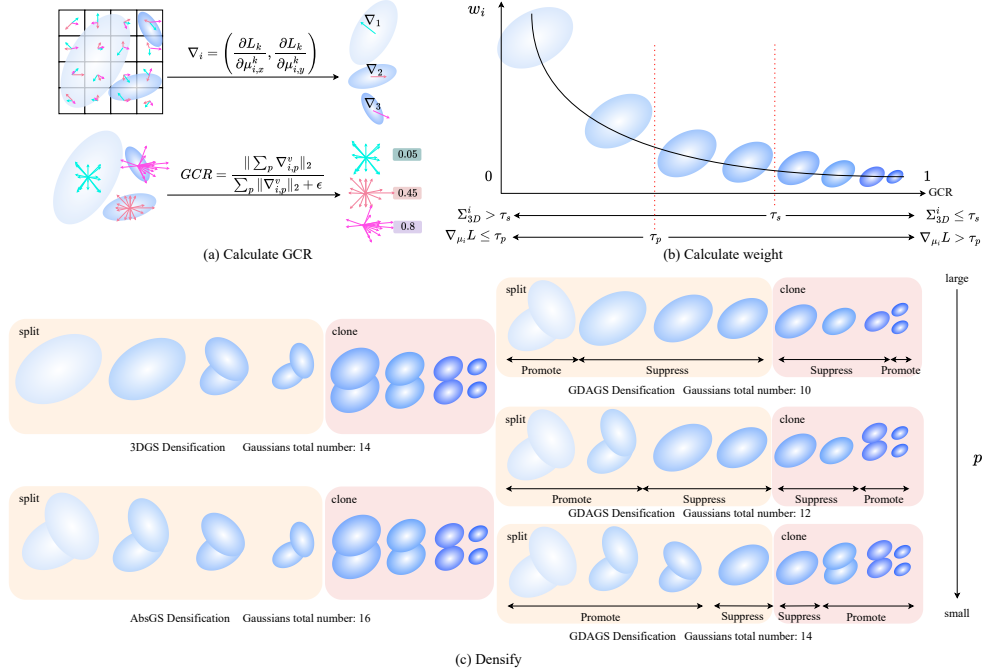


Figure 2: The pipeline of GDAGS. First, for each Gaussian, GDAGS computes the GCR to quantify the directional coherence of its subgradients. Subsequently, this GCR metric is mapped through a nonlinear dynamic weighting function to generate per-Gaussian gradient weights, which modulate the view-space positional gradient magnitudes and produce a refined decision metric. Finally, this decision metric is compared against a predefined threshold to dynamically regulate densification. The detailed algorithm pseudocode is presented in Appendix A.

3.1 Motivation

The density control mechanism in 3D Gaussian Splatting fundamentally relies on comparing view-space positional gradient norms with predefined thresholds. However, the directional characteristics of subgradients implicitly modulate these gradient norms, either attenuating or amplifying the magnitude. This manifests as undesirable phenomena, including local blurring and excessive Gaussian proliferation, ultimately degrading rendering quality. To address these limitations, we propose to explicitly incorporate subgradient directional information into a nonlinear weighting function to construct a novel decision metric for resolving over-reconstruction and over-densification issues. Specifically, during splitting operations (targeting larger Gaussians), the GCR is utilized to determine the weighting strategy: Gaussians with smaller GCR values (indicating directional conflicts) receive amplified decision metrics through nonlinear weighting, thereby prioritizing their densification. Conversely, Gaussians with larger GCR values (exhibiting directional consistency) obtain diminished decision metrics and are suppressed. In contrast, during cloning operations (targeting smaller Gaussians), the weighting mechanism is inverted: low-GCR Gaussians are suppressed while high-GCR Gaussians are promoted for densification. This is because the Gaussian clones of high GCR can smoothly move towards the gradient direction, while the Gaussian clones of low-GCR stack locally. By systematically integrating both gradient directional information and magnitude characteristics into the decision metric, GDAGS optimizes density control mechanisms. This approach not only mitigates the inherent limitations of conventional 3DGS but also significantly reduces both the required number of Gaussians and memory consumption. Additional technical details are provided in Appendix B.

3.2 Preliminary

3DGS represents scenes using a set of learnable anisotropic 3D Gaussian primitives. Each Gaussian is parameterized by a position $\mu \in \mathbb{R}^3$, an opacity $\alpha \in [0, 1]$, a covariance matrix $\Sigma \in \mathbb{R}^{3 \times 3}$, and spherical harmonics (SH) [17] coefficients for view-dependent color. The covariance matrix Σ is

decomposed into a rotation matrix R and a scaling matrix S to ensure positive semi-definiteness:

$$\Sigma = RSS^{\top}R^{\top}, \quad (1)$$

where S is a diagonal matrix parameterized by a vector $s \in (\mathbb{R}_+)^3$, and R is a rotation matrix parameterized by a quaternion $q \in \mathbb{R}^4$. The Gaussian distribution is defined as:

$$G(\mathbf{x}) = \exp\left(-\frac{1}{2}(\mathbf{x} - \mu)^{\top}\Sigma^{-1}(\mathbf{x} - \mu)\right), \quad (2)$$

where $\mathbf{x} \in \mathbb{R}^3$ is an arbitrary position.

During rendering, 3D Gaussians are projected into 2D camera space as G' , with pixel color $C(\mathbf{x}')$ computed via alpha-blending:

$$C(\mathbf{x}') = \sum_{k=1}^K c_k \alpha_k G'_k(\mathbf{x}') T_k, \quad T_k = \prod_{j=1}^{k-1} (1 - \alpha_j G'_j(\mathbf{x}')), \quad (3)$$

Here, K denotes the count of Gaussians influencing the pixel, c_k represents the view-dependent SH-based color, and α_k combines opacity with the Gaussian's spatial contribution at \mathbf{x}' .

To address sparse input from structure-from-motion (SfM) [18], a densification strategy is employed. Under-reconstructed regions (missing geometric features) are addressed by cloning Gaussians, increasing their number and volume. Over-reconstructed regions (large Gaussians covering small areas) are split into smaller Gaussians, maintaining volume but increasing count. Densification decisions are based on view-space gradients. For a Gaussian G_i with projection μ_i^k under viewpoint k and loss L_k , the average gradient magnitude is:

$$\nabla_{\mu_i} L = \frac{1}{M} \sum_{k=1}^M \sqrt{\left(\frac{\partial L_k}{\partial \mu_{i,x}^k}\right)^2 + \left(\frac{\partial L_k}{\partial \mu_{i,y}^k}\right)^2}, \quad (4)$$

where M is the number of viewpoints involved in training. Split Gaussians into smaller components if $\nabla_{\mu_i} L > \tau_p$ and $\Sigma_{3D}^i > \tau_s$. Clone Gaussians to preserve local density if $\nabla_{\mu_i} L > \tau_p$ and $\Sigma_{3D}^i \leq \tau_s$.

3.3 GDAGS

3.3.1 Directional consistency measurement

For each Gaussian observed across V views, we compute directional consistency metric GCR as \mathcal{C}_i :

$$\mathcal{C}_i = \frac{\|\sum_{pixel} \nabla_{i,pixel}^v\|_2}{\sum_{pixel} \|\nabla_{i,pixel}^v\|_2 + \epsilon}, \quad (5)$$

where $pixel$ denotes a pixel in the 2D space, and $\nabla_{i,pixel}^v \in \mathbb{R}^2$ represents the subgradient component projected onto each pixel in view v . According to the Cauchy-Schwarz Inequality $0 \leq \|\sum_{pixel} \nabla_{i,pixel}^v\|_2 \leq \sum_{pixel} \|\nabla_{i,pixel}^v\|_2$, it can be seen that the value of \mathcal{C}_i is strictly controlled between $[0,1]$, and GCR isolates the influence of gradient amplitude and only represents the consistency of gradient direction. This formulation captures:

- **High Consistency** ($\mathcal{C}_i \rightarrow 1$): Gradient directions are consistent, their magnitudes effectively accumulate.
- **Low Consistency** ($\mathcal{C}_i \rightarrow 0$): Conflicting gradient directions result in mutual cancellation of magnitudes.

The denominator $\sum_{pixel} \|\nabla_{i,pixel}^v\|_2$ captures the total gradient activity agnostic to directional variations, while the numerator $\|\sum_{pixel} \nabla_{i,pixel}^v\|_2$ quantifies the net directional alignment.

3.3.2 Nonlinear dynamic weight design

Let $\theta_{i,v} \in [0, 2\pi)$ denote the gradient direction of Gaussian i in view v , modeled as samples from a von Mises-Fisher (vMF) distribution:

$$p(\theta_{i,v}|m_i, \kappa_i) = \frac{\kappa_i}{2\pi I_0(\kappa_i)} e^{\kappa_i \cos(\theta_{i,v} - m_i)}, \quad (6)$$

where m_i is the mean direction and $\kappa_i > 0$ the concentration parameter. The empirical directional consistency \mathcal{C}_i relates to κ_i through:

$$\mathcal{C}_i = \frac{I_1(\kappa_i)}{I_0(\kappa_i)} \approx 1 - \frac{1}{2\kappa_i} + \mathcal{O}(\kappa_i^{-2}), \quad (7)$$

where I_n denotes the modified Bessel function of order n .

Then, we define the target distribution $q^*(\nabla)$ that emphasizes directionally inconsistent regions:

$$q^*(\nabla) = \frac{1}{Z} \|\nabla\|_2^{1-\mathcal{C}_i} \quad \text{with} \quad Z = \int \|\nabla\|_2^{1-\mathcal{C}_i} d\nabla, \quad (8)$$

where Z is the normalization constant. The KL divergence between empirical distribution $p(\nabla)$ and $q^*(\nabla)$ is:

$$D_{KL}(p||q^*) = \mathbb{E}_p[\log p(\nabla)] - \mathbb{E}_p[\log \|\nabla\|_2^{1-\mathcal{C}_i}] + \log Z, \quad (9)$$

Substituting the weighted distribution $p_w(\nabla) \propto w(\nabla)p_0(\nabla)$ and taking variational derivative:

$$\frac{\delta D_{KL}}{\delta w} = \frac{(1 - \mathcal{C}_i) \log \|\nabla\|_2 - \log w}{\mathbb{E}[w]} + \lambda = 0, \quad (10)$$

where λ is a Lagrange multiplier. Solving this yields the optimal weight:

$$w^*(\nabla) = \exp((1 - \mathcal{C}_i) \log \|\nabla\|_2). \quad (11)$$

For ease of use and simplification of calculations, we represent $w^*(\nabla)$ as $w_i \propto (1 - \mathcal{C}_i)$, where w_i is the weight corresponding to Gaussian G_i . Furthermore, we design w_i as follows:

$$w_i = \alpha + \beta \cdot (1 - \mathcal{C}_i)^p, \quad (12)$$

where $\alpha \in [0, 1]$ acts as a baseline suppress factor that suppresses split operations under directional consistency, while β serves as an amplification factor to enhance weight responses when directional discrepancies occur. The shape-adjustable hyperparameter p governs the nonlinearity of the weight response curve. As p increases, the curve exhibits progressively steeper gradients, which correspondingly diminish the proportion of Gaussians surpassing the split threshold. This formulation preserves three fundamental mathematical properties: monotonicity, boundedness, and convexity. For visual reference, the response curves corresponding to different p values are presented in Appendix B. The decision measurements are represented as follows:

$$\nabla_{split} = \nabla_{\mu_i} L \cdot w_i, \quad \nabla_{clone} = \nabla_{\mu_i} L / w_i. \quad (13)$$

4 Experiments

4.1 Setup

Datasets. Similar to the 3DGS dataset, we selected all 9 scenes introduced in MIP-NeRF360 [9], including indoor and outdoor scenes, Train and Trck scenes in Tanks&Temples [19], and drJohnson and playroom scenes in Deep Blending [20].

Baselines. The proposed method is benchmarked against three categories of approaches: fast NeRF frameworks (Plenoxels [3], Instant-NGP [8]), state-of-the-art NeRF-based models (Mip-NeRF360 [9]), and 3DGS variants including the widely adopted 3DGS [4], over-reconstruction-focused AbsGS [5], and Pixel-GS [16], ensuring comprehensive evaluation across all datasets.

Table 1: Quantitative comparison on three datasets. SSIM \uparrow and PSNR \uparrow are higher-the-better; LPIPS \downarrow is lower-the-better. For fair comparison and to balance the trade-off between overall quality and memory consumption, we trained these datasets with the same settings as 3DGS. All methods use the same training data for training. The **best score**, **second best score**, and **third best score** are red, orange, and yellow, respectively. **Pixel-GS*** refers to the utilization of training images within the Mip-NeRF360 dataset at the same resolution as 3DGS, as opposed to the downsampled images adopted in the original publication.

Datasets	Mip-NeRF360				Tanks&Temples				Deep Blending			
Methods	SSIM \uparrow	PSNR \uparrow	LPIPS \downarrow	Mem \downarrow	SSIM \uparrow	PSNR \uparrow	LPIPS \downarrow	Mem \downarrow	SSIM \uparrow	PSNR \uparrow	LPIPS \downarrow	Mem \downarrow
Plenoxels [3]	0.626	23.08	0.463	2.1GB	0.719	21.08	0.379	2.3GB	0.795	23.06	0.510	2.7GB
INGP [8]	0.671	25.30	0.371	13MB	0.723	21.72	0.330	13MB	0.797	23.62	0.423	13MB
Mip-NeRF360 [9]	0.792	27.69	0.237	8.6MB	0.759	22.22	0.257	8.6MB	0.901	29.40	0.245	8.6MB
3DGS [4]	0.815	27.21	0.214	734MB	0.841	23.14	0.183	411MB	0.903	29.41	0.243	676MB
Pixel-GS* [16]	0.823	27.67	0.193	1.2GB	0.853	23.74	0.150	1.05GB	0.896	28.91	0.248	1.1GB
AbsGS-0004 [5]	0.820	27.49	0.191	728MB	0.853	23.73	0.162	304MB	0.902	29.67	0.236	444MB
AbsGS-0008 [5]	0.815	27.41	0.211	450MB	0.844	23.54	0.183	202MB	0.903	29.69	0.241	380MB
GDAGS (Ours)	0.821	27.55	0.199	515MB	0.847	23.55	0.176	226MB	0.905	29.70	0.235	388MB

Implementation Details. Our experimental setup follows the original paper parameter settings of 3DGS, with densification performed every 100 iterations, stopping densification after 15k iterations and completing training at 30k iterations. The suppression factor α in the weight function is set to 0.8, the amplification factor β is set to the size threshold of 25, and the hyperparameter p is set to 15. All experiments are conducted on a single NVIDIA 4090 GPU with 24GB of graphics memory. We report the view metrics PSNR, SSIM, and LPIPS [21], and the memory used to store Gaussian parameters to demonstrate the trade-off between performance and efficiency.

4.2 Comparison

Table 2: Ablation experiment on three datasets. SSIM \uparrow and PSNR \uparrow are higher-the-better; LPIPS \downarrow is lower-the-better. The **best score**, and **second best score** are red, and orange, respectively.

Datasets	Mip-NeRF360				Tanks&Temples				Deep Blending			
Methods	SSIM \uparrow	PSNR \uparrow	LPIPS \downarrow	Mem \downarrow	SSIM \uparrow	PSNR \uparrow	LPIPS \downarrow	Mem \downarrow	SSIM \uparrow	PSNR \uparrow	LPIPS \downarrow	Mem \downarrow
3DGS	0.815	27.21	0.214	734MB	0.841	23.14	0.183	411MB	0.903	29.41	0.243	676MB
GDAGS-S	0.819	27.52	0.240	441MB	0.846	23.54	0.178	195MB	0.905	29.67	0.238	328MB
GDAGS-C	0.812	27.46	0.217	615MB	0.847	23.71	0.180	305MB	0.904	29.70	0.240	452MB
GDAGS (Ours)	0.821	27.55	0.199	515MB	0.847	23.55	0.176	226MB	0.905	29.70	0.235	388MB

Quantitative Results. We report the quantitative results of the experiment in the Table 1, which indicate that our method produces comparable results in most cases. It is worth noting that our method has less memory at performance close to or better than SOTA. Compared to Pixel-GS, GDAGS achieves comparable or superior rendering performance with only 20%-50% of the memory consumption. This, combined with its comparison against 3DGS, demonstrates that GDAGS effectively addresses over-densification through nonlinear dynamic weights that suppress redundant Gaussians during densification. By adaptively controlling density, GDAGS enables scene Gaussians to converge toward compact spatial representations. In comparisons under identical memory constraints like AbsGS-0008, GDAGS exhibits full superiority in performance. Even when competing against AbsGS-004 under larger memory budgets, GDAGS maintains comparable results. GDAGS employs direction-aware adaptive dynamic weighting for individual Gaussians, promoting effective densification while optimizing spatial representations.

Qualitative Results. We present novel view synthesis results of GDAGS and baseline methods in Figure 3, demonstrating that our approach achieves high-quality visual fidelity across all scenes while effectively mitigating localized blur and detail loss, such as vegetation under benches, uneven concrete pavements, and textural details on train surfaces. Comprehensive quantitative and qualitative results are presented in the Appendix C.

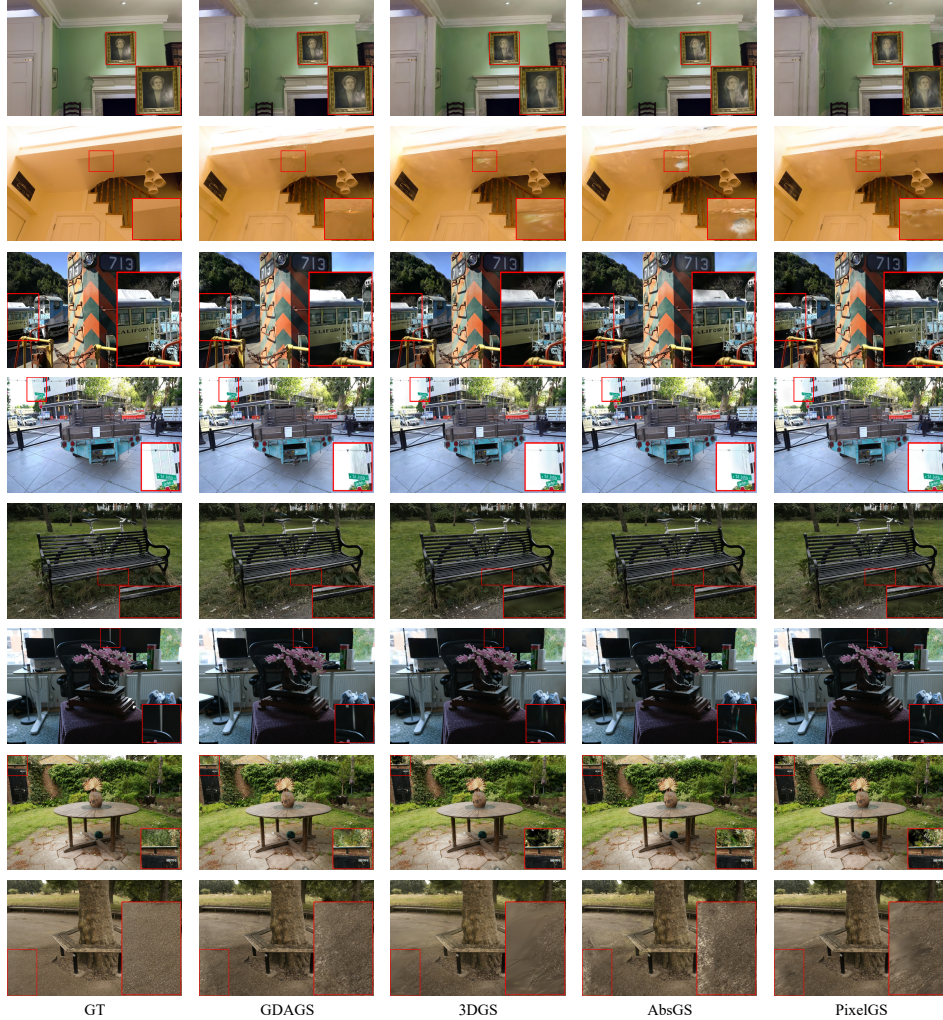


Figure 3: Qualitative comparisons of different methods on scenes from Mip-NeRF360, Tanks&Temples and Deep Blending datasets. Enlarged images are displayed in the bottom right corner.

4.3 Analysis

4.3.1 Ablation analysis

We conduct ablation experiments on the proposed weighting method and trained two additional models: GDAGS-S and GDAGS-C, which represent split gradient weighting and clone gradient weighting, respectively, for experimental comparison with the original 3DGS and complete GDAGS. The experimental results are shown in Table 2. Split gradient weighting can effectively optimize SSIM and LPIPS indicators and reduce memory costs. Clone gradient weighting can improve PSNR indicators but increase memory costs. Integrating split gradient weighting and clone gradient weighting can achieve a balance between performance and efficiency.

4.3.2 Parameter sensitivity analysis

We conduct a parameter sensitivity analysis on the hyperparameter p to reflect the impact of parameters on the model. We set the parameters to 10, 15, 20, 25, and 30, respectively, and the specific data is shown in Figure 4. In the previous analysis, we explained that the hyperparameter p controls the number of Gaussians selected for densification in adaptive density control, thereby indirectly controlling the total number of Gaussians. The increase of hyperparameter p decreases the number

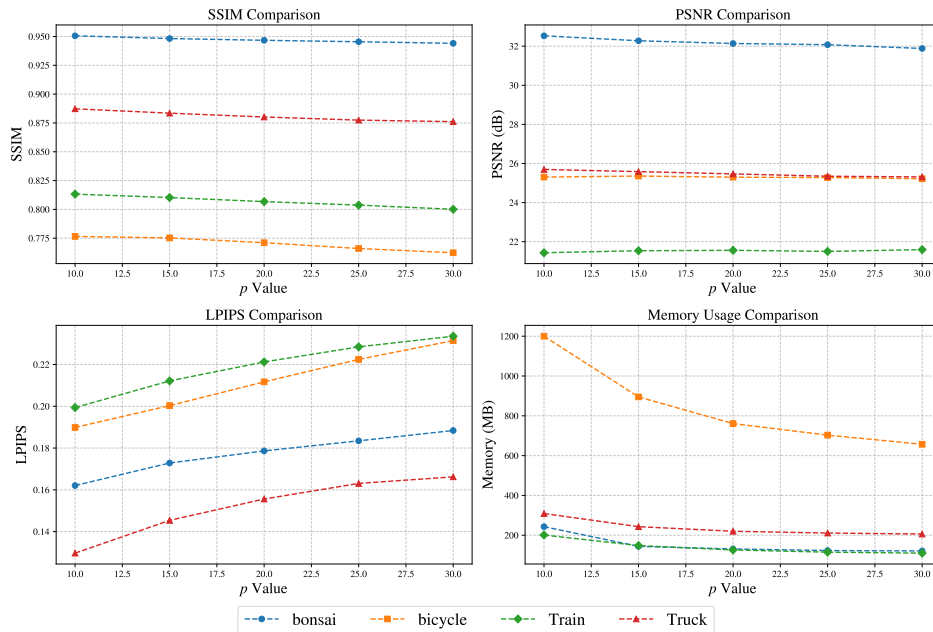


Figure 4: Performance of different hyperparameters p in multiple datasets.

of Gaussians used for densification, thereby reducing memory and lowering rendering performance. The reduction of hyperparameter p increases the number of Gaussians used for densification, thereby increasing memory and improving rendering performance.

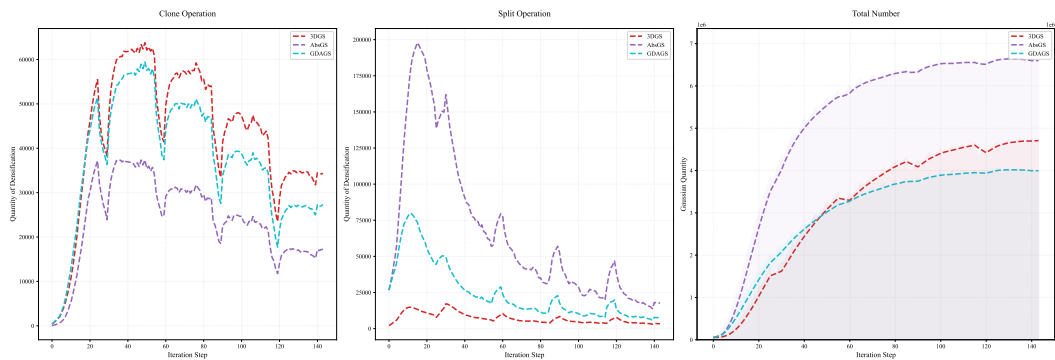


Figure 5: Visualization of different densification methods during the training process in bicycle sense.

4.3.3 Densification process analysis

We quantified the Gaussian split/clone counts per densification round and the total Gaussian population dynamics during training (see Figure 5). The experimental results demonstrate distinct behavioral patterns: In cloning operations, all three methods exhibit consistent trends, with 3DGS achieving the highest clone count due to its standard threshold. AbsGS, employing twice the cloning threshold of 3DGS, yields the lowest clone numbers, whereas GDAGS suppresses directionally inconsistent clones through gradient alignment constraints, resulting in intermediate cloning activity. GDAGS further ensures localized replenishment of directionally consistent clones while mitigating redundant accumulation of geometrically conflicting clones. For splitting operations, AbsGS generates excessive splits by indiscriminately utilizing gradient magnitudes, whereas 3DGS underperforms due to gradient direction conflicts. GDAGS effectively filters splittable Gaussians through adaptive criteria. Regarding total Gaussian counts, GDAGS exhibits a more stable trajectory and faster convergence

compared to 3DGS and AbsGS, validating its optimized densification strategy in balancing geometric fidelity and computational efficiency.

5 Conclusion

This paper proposes GDAGS, a dynamic adaptive Gaussian splatting framework that addresses critical challenges in 3D scene reconstruction, including over-densification, over-reconstruction, and memory inefficiency. By introducing the directional consistency metric (GCR) and nonlinear dynamic weighting, GDAGS enables direction-aware densification control: GCR discriminates between directionally consistent/divergent Gaussians, while dynamic weights independently regulate densification at the per-Gaussian level. This dual mechanism effectively suppresses redundant Gaussian proliferation, eliminates outlier distributions, and drives compact spatial representations without relying on heuristic threshold tuning.

References

- [1] Ben Mildenhall, Pratul P Srinivasan, Matthew Tancik, Jonathan T Barron, Ravi Ramamoorthi, and Ren Ng. Nerf: Representing scenes as neural radiance fields for view synthesis. *Communications of the ACM*, 65(1):99–106, 2021.
- [2] Dor Verbin, Peter Hedman, Ben Mildenhall, Todd Zickler, Jonathan T Barron, and Pratul P Srinivasan. Ref-nerf: Structured view-dependent appearance for neural radiance fields. In *IEEE/CVF Conference on Computer Vision and Pattern Recognition (CVPR)*, pages 5481–5490. IEEE, 2022.
- [3] Sara Fridovich-Keil, Alex Yu, Matthew Tancik, Qinhong Chen, Benjamin Recht, and Angjoo Kanazawa. Plenoxels: Radiance fields without neural networks. In *IEEE/CVF Conference on Computer Vision and Pattern Recognition (CVPR)*, pages 5501–5510, 2022.
- [4] Bernhard Kerbl, Georgios Kopanas, Thomas Leimkühler, and George Drettakis. 3d gaussian splatting for real-time radiance field rendering. *ACM Trans. Graph.*, 42(4):139–1, 2023.
- [5] Zongxin Ye, Wenyu Li, Sidun Liu, Peng Qiao, and Yong Dou. Absgs: Recovering fine details in 3d gaussian splatting. In *Proceedings of the 32nd ACM International Conference on Multimedia (ACM MM)*, pages 1053–1061, 2024.
- [6] Jonathan T Barron, Ben Mildenhall, Matthew Tancik, Peter Hedman, Ricardo Martin-Brualla, and Pratul P Srinivasan. Mip-nerf: A multiscale representation for anti-aliasing neural radiance fields. In *IEEE/CVF International Conference on Computer Vision (ICCV)*, pages 5855–5864, 2021.
- [7] Cheng Sun, Min Sun, and Hwann-Tzong Chen. Direct voxel grid optimization: Super-fast convergence for radiance fields reconstruction. In *IEEE/CVF Conference on Computer Vision and Pattern Recognition (CVPR)*, pages 5459–5469, 2022.
- [8] Thomas Müller, Alex Evans, Christoph Schied, and Alexander Keller. Instant neural graphics primitives with a multiresolution hash encoding. *ACM transactions on graphics (TOG)*, 41(4):1–15, 2022.
- [9] Jonathan T Barron, Ben Mildenhall, Dor Verbin, Pratul P Srinivasan, and Peter Hedman. Mip-nerf 360: Unbounded anti-aliased neural radiance fields. In *IEEE/CVF Conference on Computer Vision and Pattern Recognition (CVPR)*, pages 5470–5479, 2022.
- [10] Zehao Yu, Anpei Chen, Binbin Huang, Torsten Sattler, and Andreas Geiger. Mip-splatting: Alias-free 3d gaussian splatting. In *IEEE/CVF Conference on Computer Vision and Pattern Recognition (CVPR)*, pages 19447–19456, 2024.
- [11] Zehao Yu, Torsten Sattler, and Andreas Geiger. Gaussian opacity fields: Efficient adaptive surface reconstruction in unbounded scenes. *ACM Transactions on Graphics (TOG)*, 43(6):1–13, 2024.

- [12] Binbin Huang, Zehao Yu, Anpei Chen, Andreas Geiger, and Shenghua Gao. 2d gaussian splatting for geometrically accurate radiance fields. In *ACM SIGGRAPH 2024 conference papers*, pages 1–11, 2024.
- [13] Baowen Zhang, Chuan Fang, Rakesh Shrestha, Yixun Liang, Xiaoxiao Long, and Ping Tan. Rade-gs: Rasterizing depth in gaussian splatting. *arXiv preprint arXiv:2406.01467*, 2024.
- [14] Jiahui Zhang, Fangneng Zhan, Muyu Xu, Shijian Lu, and Eric Xing. Fregs: 3d gaussian splatting with progressive frequency regularization. In *IEEE/CVF Conference on Computer Vision and Pattern Recognition (CVPR)*, pages 21424–21433, 2024.
- [15] Xinpeng Liu, Zeyi Huang, Fumio Okura, and Yasuyuki Matsushita. Hogs: Unified near and far object reconstruction via homogeneous gaussian splatting. In *IEEE/CVF Conference on Computer Vision and Pattern Recognition (CVPR)*, 2025.
- [16] Zheng Zhang, Wenbo Hu, Yixing Lao, Tong He, and Hengshuang Zhao. Pixel-gs: Density control with pixel-aware gradient for 3d gaussian splatting. In *European Conference on Computer Vision (ECCV)*, pages 326–342. Springer, 2024.
- [17] George B Arfken, Hans J Weber, and Frank E Harris. *Mathematical methods for physicists: a comprehensive guide*. Academic press, 2011.
- [18] Johannes L Schonberger and Jan-Michael Frahm. Structure-from-motion revisited. In *Proceedings of the IEEE conference on computer vision and pattern recognition*, pages 4104–4113, 2016.
- [19] Peter Hedman, Julien Philip, True Price, Jan-Michael Frahm, George Drettakis, and Gabriel Brostow. Deep blending for free-viewpoint image-based rendering. *ACM Transactions on Graphics (ToG)*, 37(6):1–15, 2018.
- [20] Arno Knapitsch, Jaesik Park, Qian-Yi Zhou, and Vladlen Koltun. Tanks and temples: Benchmarking large-scale scene reconstruction. *ACM Transactions on Graphics (ToG)*, 36(4):1–13, 2017.
- [21] Richard Zhang, Phillip Isola, Alexei A Efros, Eli Shechtman, and Oliver Wang. The unreasonable effectiveness of deep features as a perceptual metric. In *IEEE/CVF Conference on Computer Vision and Pattern Recognition (CVPR)*, pages 586–595, 2018.

A Algorithm and weighted response curve

Algorithm 1 Gradient-Direction-Aware Adaptive Densityfication

Require: Gaussian set \mathcal{G} , training views \mathcal{V} , initial thresholds τ

Ensure: Optimized Gaussian set \mathcal{G}'

- 1: Initialize gradient buffers $\{\nabla_{i,v}\} \leftarrow 0$
 - 2: **for** each iteration $t = 1$ to T **do**
 - 3: **for** each view $v \in \mathcal{V}$ **do**
 - 4: Render \mathcal{G} via differentiable splatting
 - 5: Compute 2D gradient map $\sum_{pixel} \nabla_{i,pixel}^v$ and $\sum_{pixel} \|\nabla_{i,p}^v\|_2$
 - 6: Accumulate ∇_i^v for visible Gaussians
 - 7: **end for**
 - 8: **for** each Gaussian $g_i \in \mathcal{G}$ **do**
 - 9: Compute \mathcal{C}_i via Eq. (5)
 - 10: Calculate w_i using Eq. (12)
 - 11: **end for**
 - 12: Compute $\nabla_{split}, \nabla_{clone}$
 - 13: Split if $\nabla_{split} > \tau_p$ & $\Sigma_{3D}^i > \tau_s$
 - 14: Clone if $\nabla_{clone} > \tau_p$ & $\Sigma_{3D}^i \leq \tau_s$
 - 15: **end for**
-

B Gaussian densification

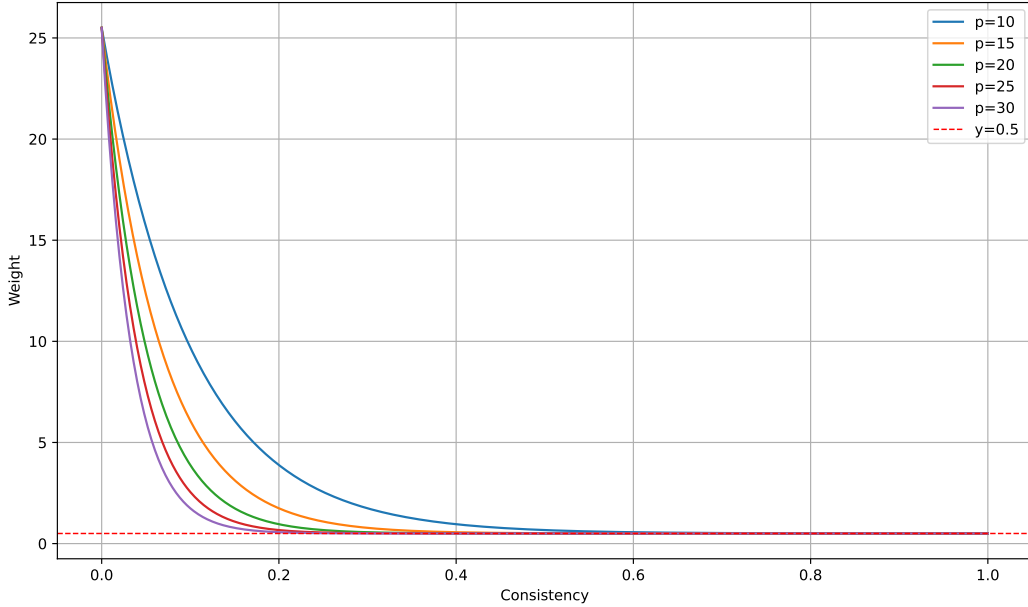


Figure 6: Corresponding curves of weights for different hyperparameters p .

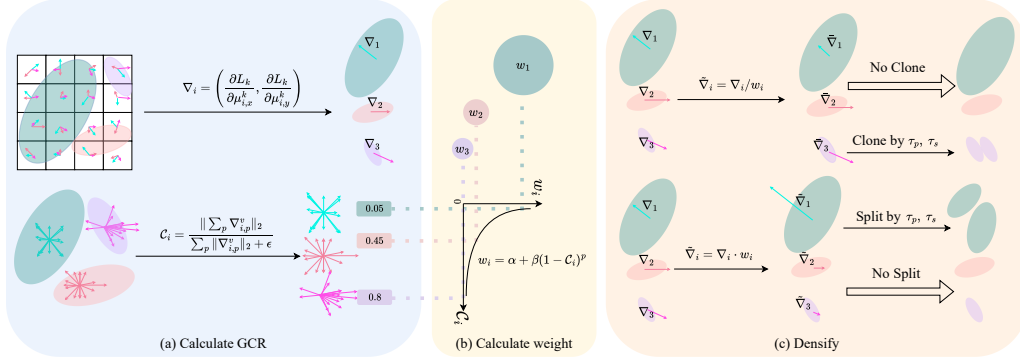


Figure 7: Comparison of more detailed methods in the Gaussian densification process.

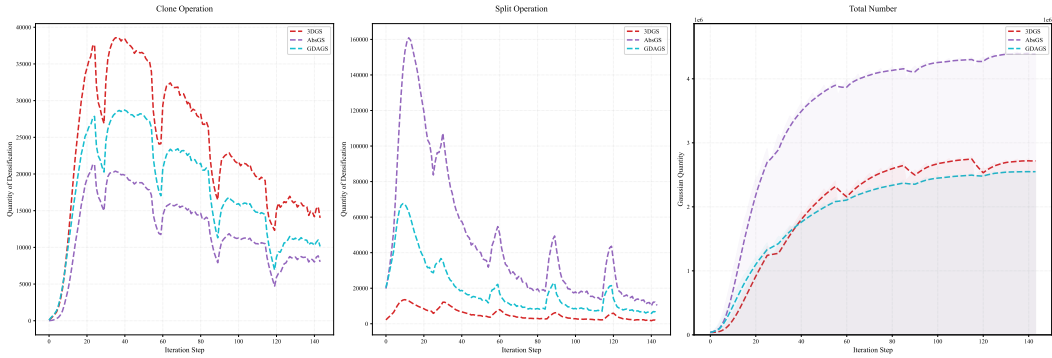


Figure 8: Visualization of different densification methods during the training process in flowers sense.

C Detailed results

The detailed performance metrics across a total of 13 different scenes from the three datasets are shown in Tables 3, 4, 5, 7, 8, and 9 while efficiency metrics are presented in Tables 6 and 10. Table 11 presents the statistical error analysis. Render quality comparisons are demonstrated in Figures 9 and 10, where significant differences are highlighted with red boxes and enlarged in the bottom-right corners. Figure 11 compares over-densification phenomena, with FPS values and the number of Gaussians annotated in the top-left corners. The comparison between nonlinear weights and linear weights is shown in the Table 12.

Table 3: Per-scene quantitative results (SSIM) from the Mip-NeRF360.

	bicycle	flowers	garden	stump	treehill	room	counter	kitchen	bonsai
Plenoxels	0.496	0.431	0.606	0.523	0.509	0.841	0.759	0.648	0.814
INGP-Base	0.491	0.450	0.649	0.574	0.518	0.855	0.798	0.818	0.890
INGP-Big	0.512	0.486	0.701	0.594	0.542	0.871	0.817	0.858	0.906
Mip-NeRF360	0.685	0.583	0.813	0.744	0.632	0.913	0.894	0.920	0.941
3D-GS	0.771	0.605	0.868	0.775	0.638	0.914	0.905	0.922	0.938
AbsGS-0004	0.782	0.613	0.870	0.784	0.626	0.920	0.908	0.929	0.944
Pixel-GS	0.766	0.627	0.862	0.784	0.638	0.929	0.921	0.936	0.951
GDAGS	0.776	0.615	0.861	0.786	0.624	0.930	0.915	0.933	0.948

Table 4: Per-scene quantitative results (PSNR) from the Mip-NeRF360.

	bicycle	flowers	garden	stump	treehill	room	counter	kitchen	bonsai
Plenoxels	21.912	20.097	23.495	20.661	22.248	27.594	23.624	23.420	24.669
INGP-Base	22.193	20.348	24.599	23.626	22.364	29.269	26.439	28.548	30.337
INGP-Big	22.171	20.652	25.069	23.466	22.373	29.690	26.691	29.479	30.685
Mip-NeRF360	24.37	21.73	26.98	26.40	22.87	31.63	29.55	32.23	33.46
3D-GS	25.246	21.520	27.410	26.550	22.490	30.632	28.700	30.317	31.980
AbsGS-0004	25.373	21.298	27.579	26.766	22.074	31.582	28.968	31.774	32.283
Pixel-GS	25.263	21.677	27.393	26.938	22.343	31.952	29.270	31.950	32.687
GDAGS	25.309	21.408	27.465	26.960	22.034	31.820	29.015	31.951	32.277

Table 5: Per-scene quantitative results (LPIPS) from the Mip-NeRF360.

	bicycle	flowers	garden	stump	treehill	room	counter	kitchen	bonsai
Plenoxels	0.506	0.521	0.386	0.503	0.540	0.4186	0.441	0.447	0.398
INGP-Base	0.487	0.481	0.312	0.450	0.489	0.301	0.342	0.254	0.227
INGP-Big	0.446	0.441	0.257	0.421	0.450	0.261	0.306	0.195	0.205
Mip-NeRF360	0.301	0.344	0.170	0.261	0.339	0.211	0.204	0.127	0.176
3D-GS	0.205	0.336	0.103	0.210	0.317	0.220	0.204	0.129	0.205
AbsGS-0004	0.186	0.295	0.104	0.202	0.297	0.216	0.198	0.124	0.194
Pixel-GS	0.206	0.288	0.111	0.208	0.301	0.188	0.166	0.109	0.167
GDAGS	0.195	0.297	0.117	0.215	0.310	0.186	0.182	0.116	0.172

Table 6: Per-scene memory consumption (MB) from the Mip-NeRF360.

	bicycle	flowers	garden	stump	treehill	room	counter	kitchen	bonsai
3D-GS*	1508	813	1073	1100	1018	397	257	412	259
Pixel-GS	2040	1660	1980	1480	1690	584	592	721	487
AbsGS-0004	1156	751	932	1021	962	234	192	249	234
GDAGS	1030	635	841	683	744	223	146	197	144

Table 7: Per-scene quantitative results (SSIM) from the Tanks & Temples and Deep Blending.

	Truck	Train	Dr Johnson	Playroom
Plenoxels	0.774	0.663	0.787	0.802
INGP-Base	0.779	0.666	0.839	0.754
INGP-Big	0.800	0.689	0.854	0.779
Mip-NeRF360	0.857	0.660	0.901	0.900
3D-GS	0.879	0.802	0.899	0.906
AbsGS-0004	0.886	0.820	0.900	0.907
Pixel-GS	0.886	0.826	0.887	0.905
GDAGS	0.884	0.811	0.901	0.909

Table 8: Per-scene quantitative results (PSNR) from the Tanks & Temples and Deep Blending.

	Truck	Train	Dr Johnson	Playroom
Plenoxels	23.221	23.221	23.142	22.980
INGP-Base	23.260	20.170	27.750	19.483
INGP-Big	23.383	20.456	28.257	21.665
Mip-NeRF360	24.912	19.523	29.140	29.657
3D-GS	25.187	21.097	28.766	30.044
AbsGS-0004	25.702	22.010	28.930	29.967
Pixel-GS	25.467	22.028	28.128	29.700
GDAGS	25.560	21.557	29.232	30.166

Table 9: Per-scene quantitative results (LPIPS) from the Tanks & Temples and Deep Blending.

	Truck	Train	Dr Johnson	Playroom
Plenoxels	0.335	0.422	0.521	0.499
INGP-Base	0.274	0.386	0.381	0.465
INGP-Big	0.249	0.360	0.352	0.428
Mip-NeRF360	0.159	0.354	0.237	0.252
3D-GS	0.148	0.218	0.244	0.241
AbsGS-0004	0.131	0.193	0.240	0.232
Pixel-GS	0.120	0.178	0.255	0.241
GDAGS	0.143	0.208	0.238	0.233

Table 10: Per-scene memory consumption (MB) from the Tanks & Temples and Deep Blending.

	Truck	Train	Dr Johnson	Playroom
3D-GS*	530	218	744	504
AbsGS-0004	419	210	457	316
Pixel-GS	1200	904	1280	881
GDAGS	277	175	416	280

Table 11: Error analysis.

Datasets	Mip-NeRF360				Tanks&Temples				Deep Blending			
	SSIM \uparrow	PSNR \uparrow	LPIPS \downarrow	Mem \downarrow	SSIM \uparrow	PSNR \uparrow	LPIPS \downarrow	Mem \downarrow	SSIM \uparrow	PSNR \uparrow	LPIPS \downarrow	Mem \downarrow
seed = 1	0.821	27.557	0.199	515MB	0.847	23.558	0.176	226MB	0.905	29.698	0.235	388MB
seed = 2	0.820	27.558	0.201	530MB	0.848	23.552	0.174	250MB	0.903	29.698	0.232	410MB
seed = 3	0.823	27.559	0.196	520MB	0.845	23.553	0.178	176MB	0.906	29.697	0.237	360MB
seed = 4	0.822	27.556	0.197	560MB	0.846	23.557	0.175	270MB	0.904	29.701	0.234	430MB
seed = 5	0.819	27.552	0.202	465MB	0.849	23.551	0.173	230MB	0.907	29.700	0.231	422MB

Table 12: The LPIPS comparison between nonlinear weights and linear weights. Linear weight set to $2 - C_i$.

	playroom	Train	bicycle	flowers
nonlinear weights	0.233	0.208	0.195	0.297
linear weights	0.238	0.210	0.218	0.340

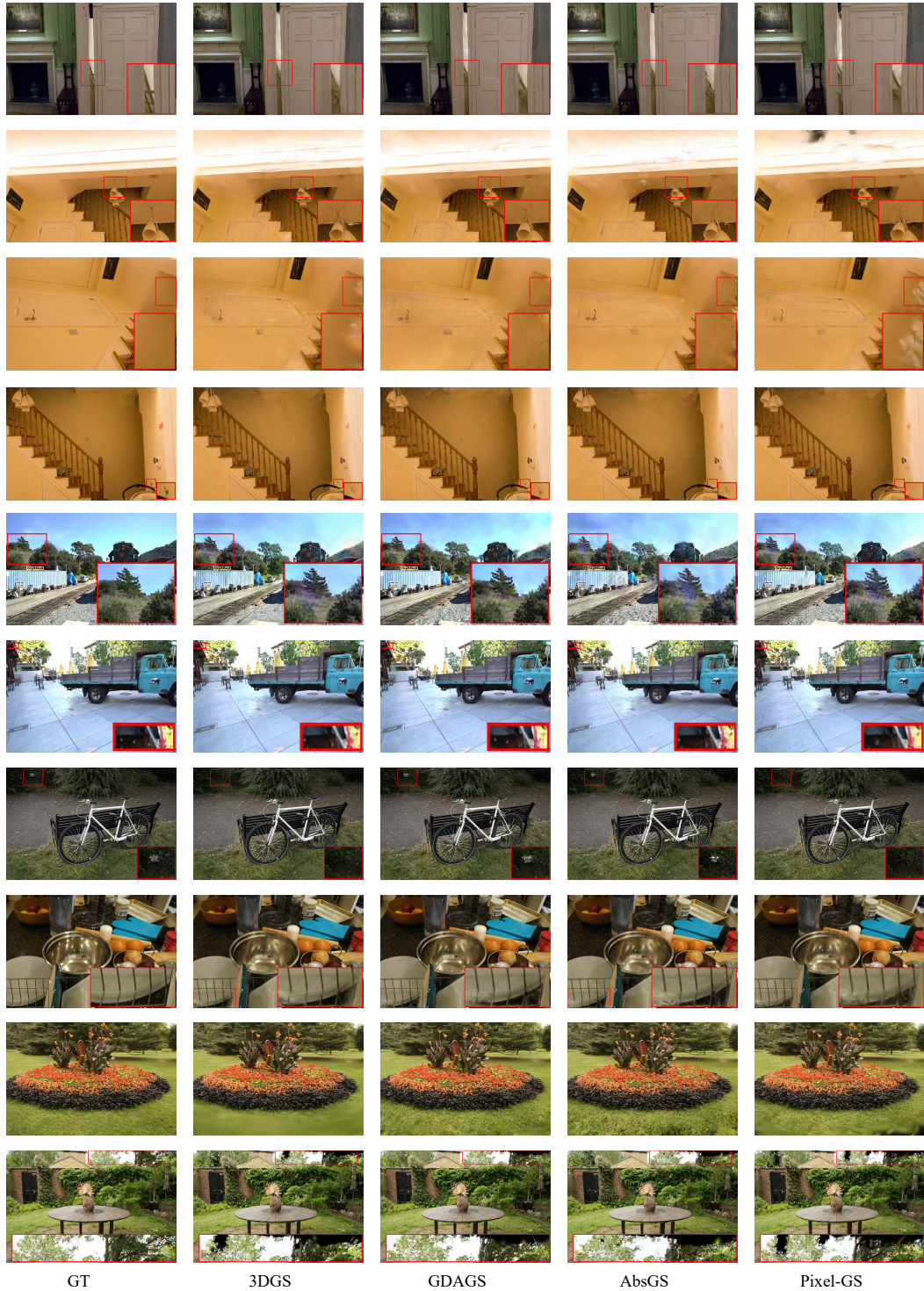


Figure 9: Supplementary qualitative analysis results.

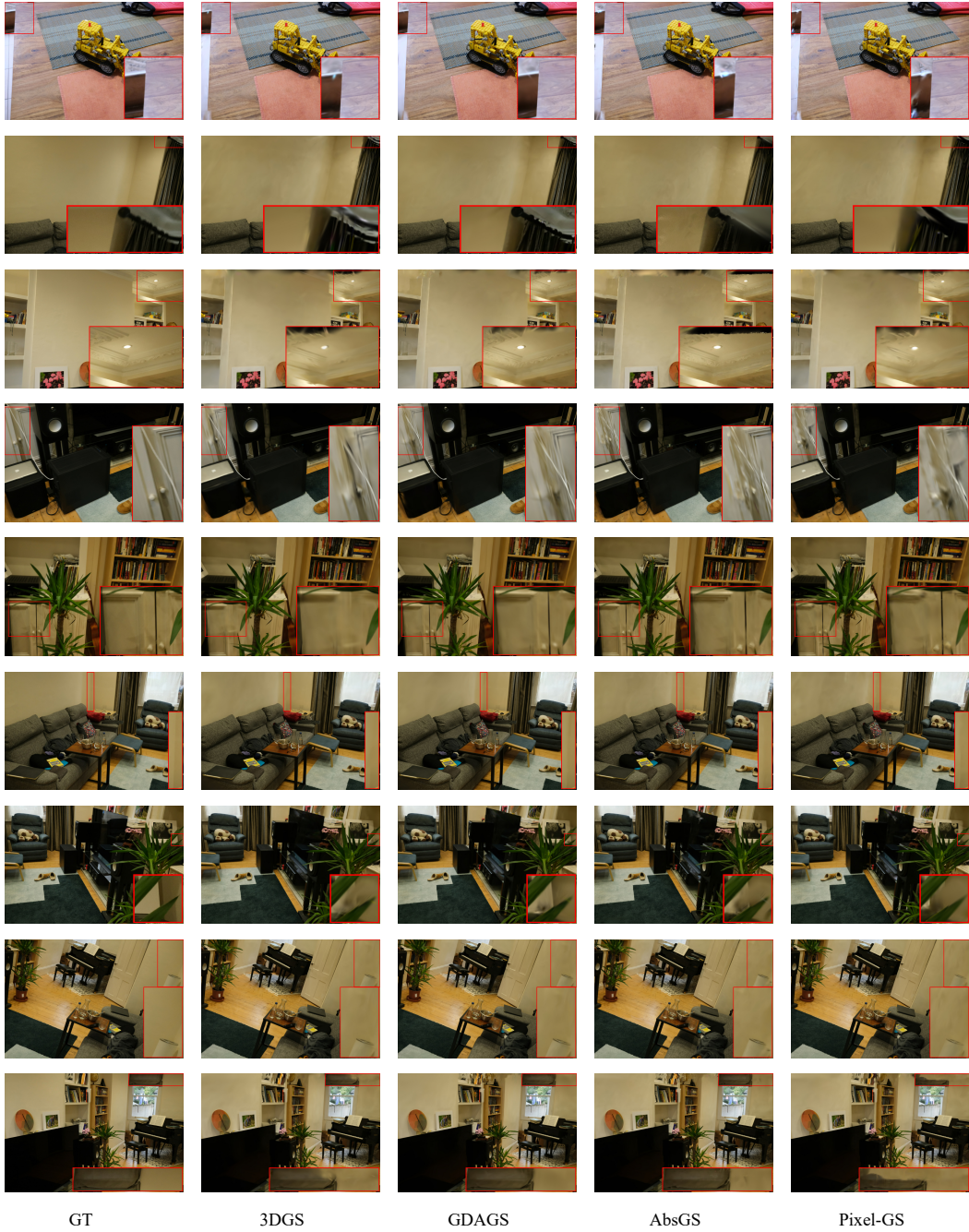


Figure 10: Supplementary qualitative analysis results.

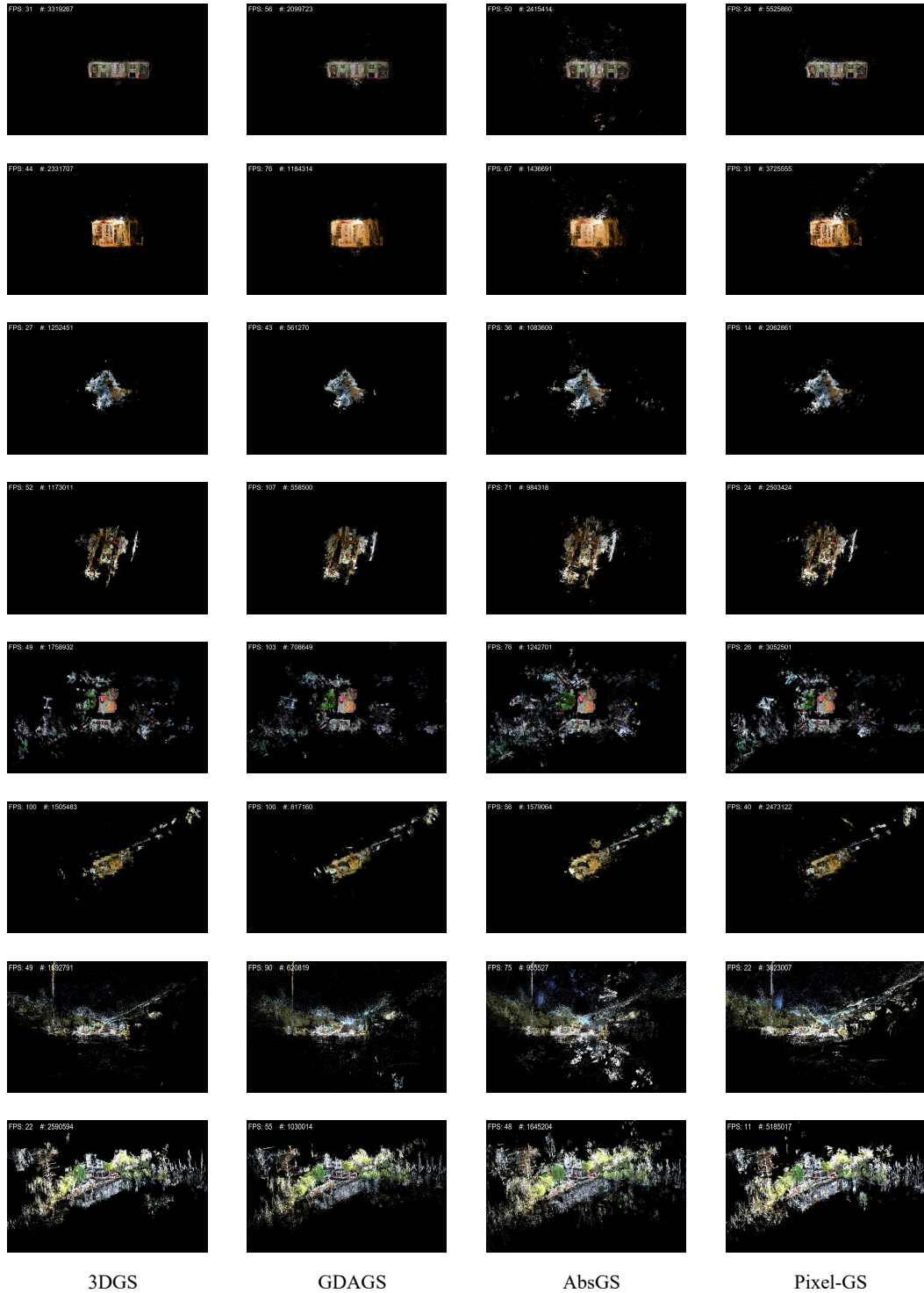


Figure 11: Comparing over-densification phenomena.

D Limitations of GDAGS

While GDAGS demonstrates significant improvements in adaptive densification control and memory efficiency, several limitations remain:

- Fixed Hyperparameters for Weighting Schemes: the hyperparameter p , which balances performance and efficiency, is fixed at 15 by default. While this value works well empirically, its optimal setting may vary across datasets or hardware configurations, requiring manual tuning for specific use cases.
- Challenges in extreme sparsity: in highly sparse regions with minimal gradient activity, GCR may struggle to distinguish between true outliers and under-reconstructed areas, leading to potential under-densification or over-suppression of Gaussians.